Feasibility of Monitoring Gas Hydrate Production with Time-Lapse VSP

M.B. Kowalsky, S. Nakagawa, and G.J. Moridis

Earth Sciences Division, Lawrence Berkeley National Laboratory, Berkeley, California

Abstract

Many studies involving the application of geophysical methods in the field of gas hydrates have focused on determining rock physics relationships for hydrate-bearing sediments, with the goal being to delineate the boundaries of gas hydrate accumulations and to estimate the quantities of gas hydrate that such accumulations contain using remote sensing techniques. However, the potential for using time-lapse geophysical methods to monitor the evolution of hydrate accumulations during production and thus to manage production has not been investigated. In this work we begin to examine the feasibility of using time-lapse seismic methods—specifically the vertical seismic profiling (VSP) method—for monitoring changes in hydrate accumulations that are predicted to occur during production of natural gas. A feasibility study of this nature is made possible through the coupled simulation of (1) large-scale production in hydrate accumulations and (2) time-lapse geophysical (seismic) surveys. We consider a hydrate accumulation in the Gulf of Mexico that may represent a promising target for production. Although the current study focuses on one seismic method (VSP), this approach can easily be extended to other geophysical methods, including other seismic methods (e.g., surface seismic or crosshole measurements) and electromagnetic surveys. In addition to examining the sensitivity of seismic attributes and parameters to the changing conditions in hydrate accumulations, our long-term goals in this work are to determine optimal sampling strategies (e.g., source frequency, time interval for data acquisition) and measurement configurations (e.g., source and receiver spacing for vertical seismic profiling), while taking into account uncertainties in rock physics relationships. The numerical modeling strategy demonstrated in this study may be used in the future to help design cost effective

geophysical surveys to track the evolution of hydrate properties. Here we describe the modeling procedure and present some preliminary results.

Introduction

Background. The ability to identify the extent of gas hydrate accumulations, predict their behavior under a variety of conditions, and monitor their properties is of great importance. Gas hydrates–solid crystalline structures consisting of water and gas molecules (usually methane)–are distributed widely across the earth in permafrost and under the ocean (Sloan, 1998). When conditions in hydrate-bearing sediment (HBS) become thermodynamically unfavorable for gas hydrates (e.g., when the pressure decreases or the temperature increases and moves the system away from the hydrate stability zone), dissociation can occur releasing large amounts of gas and water. Thus gas hydrates are viewed as a promising unconventional hydrocarbon resource (Kvenvolden, 1994; 2002), in hopes that dissociation can be induced in hydrate accumulations in a controlled manner to harvest natural gas (Makogen, 1997). The presence of HBS also serves as a hazard to hydrocarbon production platforms or infrastructure, whose integrity is at risk due to ocean floor instabilities arising from dissociation-induced submarine landslides or subsidence (Moridis and Kowalsky, 2007).

The use of geophysical methods for identifying hydrate accumulations and quantifying the amount of gas hydrates present in the subsurface has been investigated and appears promising (e.g., Hyndman and Spence, 1992; Yuan et al., 1996; Andreassen et al, 1997; Ecker et al., 1998; Ecker et al., 2000; Gueren et al. 1999), though much uncertainty remains regarding seismic (Helgerud et al., 1999; Gueren and Goldberg, 2005) and electrical (Spangenberg, 2001; Sun and Goldberg, 2005) rock physics relationships for HBS. The use of geophysical methods to remotely monitor the state of hydrate accumulations undergoing production (at distant locations where well-logging data are not available) is only beginning to be examined,

made possible by recent advances in the ability to model the complex processes which occur in such systems and which inevitably involve the nonisothermal transport of fluids and gases.

Simulation of Gas Production from Hydrate Accumulation

Numerical Simulator. We used the TOUGH+HYDRATE code (Moridis et al., 2008—hereafter referred to as T+H) to simulate gas production from the HBS we investigated in this study. T+H models the non-isothermal hydration reaction, phase behavior and flow of fluids and heat under conditions typical of natural methane–hydrate deposits in complex geological formations. It includes both equilibrium and kinetic models of hydrate formation and dissociation, and can handle any combination of hydrate dissociation mechanisms, such as depressurization, thermal stimulation and the use of inhibitors. It accounts for heat and up to four mass components (i.e., water, CH_4, hydrate, and water-soluble inhibitors such as salts or alcohols) that are partitioned among four possible phases (gas, liquid, ice or hydrate phases, existing individually or in any of 15 possible states, i.e., phase combinations). The numerical code we used to simulate seismic surveys in a hydrate accumulation before and during production is described in a subsequent section.

Geological System. The geological system we consider is similar to that described by Moridis and Reagan (2007). It is based on data collected in the Tigershark exploratory well (Smith et al., 2006) in the Alaminos Canyon Block 818 of the Gulf of Mexico, where log data indicate the presence of a sandy hydrate-bearing layer (HBL) of 18.25 m thickness, ranging from depths below the seafloor of 466 m to 485 m, with the seafloor being 2750 m below the ocean surface. The porosity ϕ is approximately 0.3, and intrinsic permeability k is on the order of 1 Darcy. The initial estimates of gas hydrate saturation S_h within the HBL, derived using resistivity and P-wave velocity data (Collett and Lee, 2006), range from 0.6 to 0.8. The

hydrate accumulations in the vicinity of this exploratory well are thought to represent technically promising targets for production since the bottom of the HBL corresponds to the bottom of the hydrate stability zone, such that dissociation may be induced in the system with relative ease (Moridis and Reagan, 2007).

Figure 1 shows the geometry of the system considered in this study (including the overlapping regions of the production and seismic simulations). The seafloor is at a depth of 0 m. Under the seafloor is 466 m of overburden, which overlies an aquifer of approximately 33.5 m thickness. The HBL, which occupies the upper 18.5 m of the aquifer, initially contains only water and hydrate (hydrate saturation S_h = 0.7, water saturation S_a = 0.3, and gas saturation S_g = 0). The remaining lower 15 m of the aquifer is initially water saturated (S_a = 1). Below the aquifer is 100 m of underburden.

The grid for the production simulation spans a vertical distance of 100 m (between depths of 433 m and 533 m), and a horizontal radius of 800 m. For the purposes of the production simulation, the overburden and underburden are assumed to allow heat exchange while being impermeable to fluid flow. The production simulation assumes cylindrical symmetry around the production well. Grid spacing in the radial direction is fine (0.25 m) near the well, and increases (to 30 m) at larger distances from the well, while vertical grid spacing is fine (0.25 m) in the HBL and increases (to 7 m) in the overburden and underburden.

An equilibrium reaction model was employed in the simulation in accordance with previous studies that indicate that this reaction model—instead of the more computationally intensive kinetic one—is justified in geological settings similar to the one considered here (Kowalsky and Moridis, 2007).

As a first step in the simulation, an equilibration procedure was performed, based on the process described by Moridis et al. (2007), to obtain appropriate initial conditions for the pressure and temperature distributions (Moridis and Reagan, 2007). The simulation of

production then proceeded by specifying the extraction of water at a constant rate from just below the HBL while providing a limited amount of electrical heating at the wellbore. Warm ocean water was also injected after a cavitation event occurred due to the formation of secondary hydrate near the wellbore. This production scenario corresponds to the best-performing wellbore design and production strategy (referred to as Case C in their notation) of the several that Moridis and Reagan (2007) investigated.

System Behavior during Production. The focus of this paper is on predicting the geophysical response during production of gas from the hydrate accumulation described above. A detailed description of the system behavior was given by Moridis and Reagan (2007); the features that are most relevant to the current study are described in this section.

In Figure 2 the evolution of S_h (Figure 2a-f) and S_g (Figure 2g-l) in and below the HBL are shown for increasing times after the start of production (0, 2, 6, 10, 14, and 18 months, respectively). Soon after the start of production, three moving dissociation fronts form within the HBL. One of the dissociation fronts moves in the radial direction and is confined to relatively small distances from the wellbore. (This near-wellbore behavior is important as it determines the overall production performance in the reservoir. However, the resulting near-wellbore properties are not of particular relevance in this study, since the geophysical surveys are conducted at 100s of meters from the wellbore). In addition, there is a descending dissociation front at the upper boundary of the HBL, and an ascending dissociation front at the lower boundary of the HBL, both extending horizontally over the entire distance of the production model.

As the HBL undergoes dissociation, S_h decreases while S_g and S_a (= $1 - S_h - S_a$) increase. The average value of S_h within the HBL decreases with time from the initial value of 0.7 to around 0.65. The largest accumulation of gas (highest values of S_g) occurs just above the top

of the HBL (see Figure 2g-l), while gas is seen to increase below the HBL as well. S_g also increases within the HBL as gas migrates upward.

These changes of physical properties observed in the HBL bode well for the application of geophysical monitoring techniques and provide motivation for the time-lapse geophysical simulations considered in this study.

Simulation of Time-Lapse Geophysical Measurements

Numerical Simulator. Full-scale 3-D simulations of seismic wave propagation reservoirs can be very computationally expensive and are not performed in the current study. Instead, we carry out 2-D seismic simulations in a small section of the reservoir, away from the production borehole, assuming incident plane P waves. To simulate seismic measurements, the wave equations for an isotropic linear viscoelastic medium (Carcione et al., 1988) are solved numerically in 2-D using a time-domain staggered-grid finite difference formulation (Levander, 1988) with calculations accurate to the fourth order in space and second order in time. While a viscoelastic code was chosen in order to allow for the effects of frequency-dependent attenuation to be modeled (Xu and McMechan, 1998), at present we focus on the elastic case in which intrinsic attenuation is not considered.

The input for the seismic simulations includes the bulk density, and the bulk and shear moduli (and additional information specifying relaxation mechanisms if intrinsic attenuation were to be modeled). The bulk density is a function of the density of the aqueous, gas, and hydrate phases, which is calculated in T+H as a function of pressure and temperature. The bulk and shear moduli are determined using a rock physics model for HBS, described below.

Overview of Rock Physics Models. In the current work, we aim to examine the sensitivity of geophysical measurements to changes in a hydrate accumulations brought about by

depressurization-induced production of methane gas. To simulate the geophysical responses, relationships are needed for calculating the elastic moduli of HBS as a function of the aqueous, gas and hydrate phase saturations; porosity; pressure; and temperature; all of which are simulated as a function of space and time in the T+H production model (described above). Due to a lack of data, there is presently no consensus on how best to model the elastic properties of HBS. For the purpose of this study it is sufficient to consider the response of several possible rock physics models. The relationships we use are described after a brief overview, given next, of empirical (Lee et al., 1996) and rock physics-based models (Helgerud et al., 1999; Carcione and Tinivella, 2000) that have been reported in literature.

Some empirical relationships for the elastic properties of HBS have been considered, such as the time-average equation (Wyllie et al., 1958) and the Wood equation (Wood, 1941), and a weighted average of the two (Lee et al., 1996). The use of rock physics models may be more widely applicable than such empirical relationships (Dvorkin et al., 2003), but they require information about how hydrate is distributed in pore space and how it affects the pore fluid and sediment frame (which has been difficult to determine due to the inherent instability of HBS when removed from in-situ conditions, and due to the variability in properties of HBS constructed in the laboratory).

Dvorkin et al. (2000) formulated an effective medium model for HBS with three cases in which gas hydrate is assumed to be either part of the pore fluid (thus affecting the elastic moduli of the fluid), part of the solid phase (hydrate acts as a component of the load-bearing sediment), or (intergranular) contact cement (hydrate affects the load-bearing component of the sediment but acts at the grain contacts). Various studies attempted to infer which of these hydrate configurations was most accurate by comparing predictions made with the models to field data, usually sonic logs. While analysis of geophysical logs collected at the Blake Ridge pointed toward hydrate acting as intergranular cement (Gueren et al., 1999), analysis of

seismic AVO data at a different location suggested that hydrate was forming in the pore space away from grain contacts (Ecker et al., 1996). In later work Ecker et al. (2000) assumed that the upper and lower bounds for estimating hydrate saturation could be determined by assuming two models (that hydrate is part of the pore fluid in one model and that it is part of the solid phase in another). A different approach was used to interpret well logging and VSP data (Carcione and Gei, 2004) based on an approach that assumes similarity between frozen porous media and hydrate sediments, using a Biot-type three-phase theory that considers the existence of two solids (grain and ice or clathrate) and a liquid. Their model assumes cementation of the grains by hydrate. Another approach was given by Lee (2002) that uses the Biot-Gassmann theory while assuming a relationship between the P- and S-wave velocities.

There is some indication from laboratory experiments that the pore-scale hydrate distribution depends on the geological setting, the conditions prevalent during hydrate formation, and on hydrate saturation. Waite et al. (2004) considered laboratory-constructed samples of unconsolidated HBS that were partially saturated with water and methane gas. They found that measured P-wave speeds were best predicted, out of four possible types of hydrate distribution, with a model in which the hydrate surrounds and cements grains. Winters et al. (2007) showed that hydrate forming in the presence of methane gas is more likely to cement coarse-grained sediment than hydrate forming in the presence of dissolved methane. Using tetrahydrofuran (THF) hydrate, an analog to natural methane hydrates, Yun et al. (2005) inferred from ultrasonic measurements that the hydrate formation mechanism seems to follow neither a pure cementation model nor a pore filling model.

It is relatively well established that the presence of gas hydrates affects seismic attenuation, but the mechanism appears to be complex and is incompletely understood (Guerin and Goldberg, 2002; 2005; Lee, 2007). It appears that in water-saturated systems

(free of methane gas) attenuation decreases as the gas hydrate saturation increases (Rossi et al., 2007). Guerin and Goldberg (2005) adapted Biot (1956) theory to account for the interactions between gas hydrate and the host sediment in order to better understand attenuation in HBS. They extended an existing model that was developed for frozen porous media (Leclaire et al., 1994) to HBS (Guerin and Goldberg, 2002), and tried to identify whether various mechanisms, such as friction, intertial coupling, cementation, and squirt flow were the main mechanisms for energy dissipation in HBS. It is expected that the introduction of substantial amounts of gas to the pore space, which is predicted to occur over large regions during production, will increase attenuation substantially.

Note that many of the rock physics models in literature, developed with the motivation of detecting natural hydrate accumulations, considered only the aqueous and gas-hydrate phase constituents in the pore space. However, the coexistence of hydrate and gas has been observed in naturally occurring hydrate accumulations (Gueren et al., 1999). Moreover, as noted above, gas saturation is expected to increase substantially during production (Figure 2). Since the presence of gas in hydrate accumulations is expected to have a dramatic effect on the seismic response (especially for P waves), the presence of gas must be accounted for in the rock physics models employed in this study.

Procedure for Calculating Elastic Moduli. In this work we follow an approach similar to that laid out by Helgerud et al. (1999) to calculate the effective bulk modulus (K_{eff}) and shear modulus (G_{eff}) of a sediment containing solid grains partially saturated by methane gas, gas hydrate, and water (any effect of dissolved methane on the elastic properties of the sediment is neglected). We do not include the ice phase, since ice does not form in the production simulation considered in this study.

The approach we employ consists of the following three steps: (1) Calculate the effective moduli of the sediment grain (K_s and G_s) by taking Hill's (1952) average of the moduli of the individual solid components (the mean of the arithmetic and harmonic averages weighted by the volumetric fractions of the solid components). As described below, Cases C and D consider the hydrate component as one of the solid components; its moduli are included in the calculation of K_s and G_s for these cases only. (2) Calculate the moduli of the dry matrix of the marine sediments (K_{dry} and G_{dry}) using the approach of Dvorkin et al. (1999). Though the details are not discussed here, these expressions are a function of K_s and G_s and the effective pressure (difference between the lithostatic and pore fluid pressure), in addition to some mineralogical parameters. (3) Calculate the effective moduli for the sand/gas/water/hydrate mixture with the effect of the hydrate on the mixture modeled using the following approaches (Cases A-D).

Case A: Hydrate Considered as Pore-Fluid Component (Uniform Gas Distribution). Gas hydrate is considered a component of the pore fluids in calculating the elastic properties, and any gas and water are assumed to be distributed uniformly within the pore space. The bulk modulus of the pore fluid K_f is determined by taking the Ruess (1929) average of the gas, aqueous and hydrate moduli:

$$K_f = \left[\frac{S_a}{K_a} + \frac{S_g}{K_g} + \frac{S_h}{K_h} \right]^{-1} \quad (1)$$

The effective bulk modulus of the solid-grain/gas/aqueous/hydrate mixture (K_{eff}) is then calculated using Gassmann's (1951) equation, which is a function of K_s, K_{dry}, K_f and porosity. In this case the shear modulus is the same as that of the dry marine sediments ($G_{eff} = G_{dry}$).

Case B: Hydrate Considered as Pore-Fluid Component (Patchy Gas Distribution). As in Case A, gas hydrate is considered a component of pore fluids in calculating the elastic properties. However, in this case, rather than being uniformly mixed within the pore space,

the gas phase is assumed to be distributed in "patches" that are on average much larger than the size of the pores. Calculation of K_{eff} is done in several steps. First, the effective bulk modulus of the sediment mixture fully saturated with the aqueous and hydrate phase ($K_{eff,a+h}$) is calculated using Gassmann's (1951) equation with the bulk modulus of the pore fluid K_f determined by taking the Ruess (1929) average of only the aqueous and hydrate moduli:

$$K_f = \left[\frac{S_a}{S_a + S_h} \cdot \frac{1}{K_a} + \frac{S_h}{S_a + S_h} \cdot \frac{1}{K_h} \right]^{-1} \tag{2}$$

Second, the effective bulk modulus of the sediment mixture fully saturated with the gas phase ($K_{eff,g}$) is calculated using Gassmann's (1951) equation with $K_f = K_g$. Then, K_{eff} for the sand/gas/aqueous/hydrate mixture is calculated using the patchy gas model of Dvorkin and Nur (1998) modified as follows to include hydrate as a pore-fluid component:

$$\frac{1}{K_{eff} + 4/3\, G_{eff}} = \frac{F_{a+h}}{K_{eff,a+h} + 4/3\, G_{eff}} + \frac{1 - F_{a+h}}{K_{eff,g} + 4/3\, G_{eff}} \tag{3}$$

where F_{a+h} is the volume of the aqueous- and hydrate-phase components divided by the total volume of the hydrate-, aqueous- and gas-phase components. Note that in this case the shear modulus is the same as that of the dry marine sediments ($G_{eff} = G_{dry}$) calculated in step 2.

Case C: Hydrate Considered as Solid-Phase Component (Uniform Gas Distribution). Gas hydrate is assumed to act as a solid-phase component in a similar manner as the solid grains of the sediment, thus affecting the calculation of K_s and G_s, which are now calculated by including the hydrate component as one of the solid components, with weighting for each component in the average equal to its volume divided by the total volume of the solid-phase components. The porosity decreases accordingly with increasing S_h, and vice versa. The bulk

modulus of the pore fluid is now determined by taking the Ruess (1929) average of only the gas and aqueous components, with the weights proportional to the volume of each component divided by the total volume of the gas and aqueous components:

$$K_f = \left[\frac{S_a}{S_a + S_g} \cdot \frac{1}{K_a} + \frac{S_g}{S_a + S_g} \cdot \frac{1}{K_g} \right]^{-1} \tag{4}$$

The calculation of K_{eff} is then done similarly to Case A using the Gassmann's (1951) equation, but with the newly calculated values of K_f and K_s. G_{eff} equals G_{dry} and is now a function of S_h.

Case D: Hydrate Considered as Solid-Phase Component (Patchy Gas Distribution). As in Case C, gas hydrate is assumed to act as a solid-phase component affecting the values of K_s and G_s. However, in this case, the distribution of methane gas is assumed to patchy rather than uniformly mixed within the pore space (see Case B). The patchy gas model of Dvorkin and Nur (1998) is again used to calculate K_{eff} , but in this case without that hydrate contributing to the pore fluid:

$$\frac{1}{K_{eff} + \frac{4}{3} G_{eff}} = \frac{F_a}{K_{eff,a} + \frac{4}{3} G_{eff}} + \frac{1 - F_a}{K_{eff,g} + \frac{4}{3} G_{eff}} \tag{5}$$

where F_a is the volume of the aqueous-phase component divided by the total volume of the aqueous- and gas-phase components. As in Case C, G_{eff} equals G_{dry} and is now a function of S_h. In this case $K_{eff,a}$ is the effective bulk modulus of the sediment mixture fully saturated with the aqueous phase, which is calculated using Gassmann's (1951) equation with the bulk modulus of the pore fluid K_f simply equal to that of the aqueous phase. As in Case B, the

effective bulk modulus of the sediment mixture fully saturated with the gas phase ($K_{eff,g}$) is calculated using Gassmann's (1951) equation with $K_f = K_g$.

An example of the seismic velocities for Cases A-D calculated using the steps described above is shown in Figure 3. In each case V_p is highest when the sediment contains only water and hydrate (S_g=0); V_p increases as water-filled pore space is replaced by hydrate (as S_a goes from 1 to 0 and S_g remains equal to 0). However, when gas enters the pore space, V_p decreases substantially for all cases with a slope depending on the case and on S_a.

Figure 4 shows how the saturation of gas hydrate in the original pore space affects V_p. When no gas is present (Figure 4a), V_p increases less rapidly for the cases in which gas hydrate only affects the elastic properties of the pore fluid (Cases A and B) compared to the cases in which gas hydrate affects the elastic properties of the sediment frame (Cases C and D). Filling the pore space with only 5% of methane gas (S_g=0.05) (Figure 4b) causes a dramatic decrease in velocity, relative to the gas-free case, at low hydrate saturation for the uniformly mixed gas cases (Cases A and C), but only very minor decrease in velocity for the patchy gas cases (Cases B and D). A notable feature for the rock physics model in Case A is the very low sensitivity of V_p to S_g when a small amount of gas is present (Figure 4b).

In Cases A and B the presence of hydrate does not affect the shear modulus (G_{eff} remains 0 regardless of S_h). However, V_s varies slightly due to changes in the bulk density (V_s decreases with increasing density). In contrast, in Cases C and D for which hydrate is modeled as a component of the solid sediment frame, V_s is affected substantially by the presence of hydrate, as described above. Accordingly, Figure 5 shows how V_s varies with S_h, with the highest value occurring at maximum hydrate saturation (S_a=S_g=0). Note that the elastic properties in Cases C and D are modeled by assuming that hydrate is not part of the pore space but part of the solid matrix. Although this should always result in—by definition—no hydrate present in the pore space, we plotted the velocities against "hydrate saturation",

defined as the volume of hydrate within the remaining hydrate-free pore space (i.e., $S_h=V_h/(V_a+V_g+V_h)$), in Figure 3 for comparison with the previous cases.

Since the purpose of this paper is to examine the effect of the HBL on seismic measurements, we are neglecting the effect of mineralogy and of the pressure and porosity gradients on the elastic moduli of the overburden and underburden. It should be noted that, in reality, velocities of HBS may follow some combination of the rock physics models described above. In addition, when calculating the effective pressure—defined as the difference between the lithostatic and pore pressure—within the HBL, we neglect variation in the lithostatic pressure throughout the 18 meter thick HBL, setting the value equal to that at the top of the HBL. Also, we are assuming that the materials can be modeled with isotropic (not anisotropic) viscoelastic properties, and that conditions on the ocean bottom are the same for all survey times.

Overall, Figures 3-5 indicate that during production of natural gas from HBS, in which gas is released and the various phase saturations change, the elastic moduli (and therefore wave velocities) can change considerably. However, the degree of change predicted by the different rock physics models varies significantly. Case A serves as the lower limit of the expected velocity values, and Case D serves as the upper limit.

Evolution of the P-wave and S-wave velocity profiles during production are shown—for a vertical slice located 650 m from the production well—in Figure 6 for rock physics model Cases A-D. As production from the HBL progresses, S-wave velocities within the entire reservoir (i.e., from the top of the HBL at 466 m to the bottom of the underlying aquifer at 500 m) increase. The overall increase is caused by the increasing effective stress from reservoir depressurization. The ratio of the velocity increase in the HBL for Cases A and B (~40%) is larger than for Cases C and D (~25%), because the sediment frame stiffness

cemented by hydrate is less sensitive to the pressure changes, and because part of the (hydrate) cement is lost in dissociation.

For P-waves, the gas introduced into the reservoir from dissociation additionally affects velocity. For Cases A and C, the frame stiffening effect owing to the increasing effective stress is surpassed by the increasing compliance of the gas-containing pore fluid, resulting in overall decreased P-wave velocities. Reduction of P-wave velocities is less pronounced for Cases B and D where the distribution of the gas is assumed to be patchy (see comparison between Figures 4a and 4b). Note that because the density changes resulting from hydrate formation/dissociation and gas production are small (less than 2% of the initial values), the corresponding seismic impedance profiles (not shown) are nearly identical to the profiles in Figure 6 (modified by a factor of the density). These changes in seismic P-wave and S-wave velocities and impedances affect the amplitudes and travel times of the simulated seismic measurements, as is described below.

Description of Seismic Simulations. The model domain for the seismic simulations in this study spans 1,100 meters by 600 meters and overlaps the production model. Rather than simulating wave propagation along the entire distance from the ocean to the HBL (and below), we focus on a region near the HBL instead, simulating an incoming P-wave (plane wave) at a given angle of incidence and recording the seismic response at a string of receivers. To achieve the desired angle of incidence, the seismic model is rotated relative to the production model (the example in Figure 1 depicts a 20 degree angle of incidence). The seismic source has a central frequency of 50 kHz, implemented by specifying the particle velocity as a Ricker wavelet. Discretization in time and space is 0.3 ms and 2 meters, respectively.

The two seismic survey configurations that are typically most useful for surveying oil and gas reservoirs in marine environments are surface reflection surveys and vertical seismic profiling (VSP) surveys. In surface reflection surveys, receivers are commonly towed in the ocean, or they can rest on the seafloor (if the seafloor is relatively shallow). This survey type is commonly used for reservoir imaging, and it can be repeated in time to provide time-lapse data that are useful for detecting small changes in subsurface properties. However, reflection surveys suffer from a number of limitations including a difficulty in reproducing source and receiver locations and coupling conditions at different survey times; a low signal-to-noise ratio; and low frequency content (and thus image resolution). In this paper, we instead consider the VSP configuration, which overcomes some of the difficulties inherent to surface reflection surveys by placing a string of receivers in a well. The use of fixed receivers in a well provides increased frequency content, better vertical and lateral resolution of the reservoir image, and an improved signal-to-noise ratio, which should allow for smaller dynamic changes in the reservoir to be detected, and to be detected more accurately (O'Brien et al., 2004). Drawbacks to this method are that a well or borehole must be present in the vicinity of the subsurface region of interest, and the information gained will be limited to a smaller region (in the vicinity of the well), though at higher resolution.

Here we employ a VSP measurement configuration with a string of 26 receivers, situated in a borehole located 650 meters from the production well, with 12.5 m spacing at depths ranging from 280 m to 592.5 m below the seafloor. This configuration allows for the seismic energy reflected off the HBL and transmitted through the HBL to be recorded and analyzed.

Since the magnitude and character of reflected and transmitted energy in a VSP survey depends on the angle of incidence of the source, in the following examples we examine two cases: one in which the source is normally incident or relative to vertical (i.e., the source is directly above the receiver well), and the other in which the source is 20 degrees from vertical

(i.e., the source is located some horizontal distance away from the receiver well). These two examples correspond to the seismic grid being rotated relative to the production grid by $\alpha = 0$ and 20 degrees, respectively (see Figure 1).

Example 1: Incoming Seismic Wave with 0^o Angle of Incidence

Here we focus on early stages of production and present simulation results for the first 20 months. As discussed above, during this period the hydrate layer changes in a complex manner. The prominent characteristics observed in this simulation are: (1) development of a laterally moving dissociation front near the producing well; (2) development of a descending dissociation front at the top of the HBL; (3) development of an ascending dissociation front at the bottom of the HBL; (4) a decreasing average value of S_h within the HBL; and (5) accumulation of gas above, below and within with HBL. With the exception of the first effect (the dissociation front moving laterally away from the production well but confined to near-well distances), the remaining dissociation behaviors, illustrated in Figure 2, are expected to affect the elastic properties in a way that is conducive to seismic monitoring in these examples. For example, the thickness of the HBL changes with time, and in so doing moves the position of seismic reflectors. The accumulation of gas affects the seismic impedance of the reflector. And the elastic moduli within the HBL change due to the varying gas saturation (Figures 3-6).

In this first example we examine the signal obtained in a vertical string of receivers for an incoming seismic wave that is normally incident to the HBL. A comparison of the waveforms simulated before and 20 months after the start of production is shown for one rock physics model (Case A) in Figure 7. Recall that the receivers at depths of 467.5 m and 480 m are in the HBL and the receiver at 492.2 is in the aquifer underneath the HBL. The first arriving energy is the direct P-wave. Changes in the direct P-wave amplitude and velocity are minimal

after one year of production. The P-wave is the only arrival that reaches the receivers below the HBL for this VSP configuration. However, another arrival is recorded at the receivers above the HBL, namely the reflected P-wave. The reflected P-wave is generated by a reflection at the HBL and arrives after the direct P-wave. Figure 8 shows the reflected P-wave recorded above the HBL at a depth of 355 m for each of the four rock physics models (Cases A-D). The simulated waveforms are shown at six survey times (0, 4, 8, 12, 16, and 20 months after the start of production), and can be seen to vary significantly throughout the hydrate production simulation. Note that the dominant wavelength for this example is approximately 50 m, and the limits of resolution (one quarter of the wavelength or ~15 meters) are on the order of the thickness of the HBL (~18 meters). Therefore, the reflected waveforms consist of a direct reflection from the top of the layer as well as complex, multiply scattered waves within the entire HBL and possibly the underlying aquifer.

The amplitudes of the reflected P-wave from the waveforms shown in Figure 8 were also calculated (Figure 9). Because no gas phase is present before production begins (at 0 months), the amplitudes for Cases A and B are the same, as are those for Cases C and D. The amplitude is larger for Cases C and D because the contrast in V_p (and the P-wave seismic impedance) between the hydrate-free background material and the HBL (S_h=0.7) is larger for these cases (see Figure 4a). With the addition of a small amount of gas to the HBL, V_p decreases in all four cases. By comparing the velocities shown in Figure 4a and 4b (at S_h=0.7), the most significant reduction of V_p is expected for Case A, followed by Case C. In contrast, Cases C and D show only very small changes. Since a reduction of velocity results in a reduced seismic impedance contrast between the background and the HBL, when the simulated waveforms in Figure 6 are examined at increased times, it is not surprising that the reflection amplitude decreases most for Case A. The waveforms for the remaining cases

change slightly with increasing survey time, but arguably not substantially enough to detect that changes have occurred in the HBL.

Changes in the transmitted P-wave recorded below the HBL at a depth of 592.5 m are minimal for all rock physics models for the duration of the production simulation (not shown).

For a normally incident VSP measurement, the amplitude of the reflected P-wave changes somewhat significantly for one of the considered rock physics models, while the transmitted P-wave arrival remains nearly constant during the production simulation. The next example considers a VSP configuration that is expected to be more sensitive to changes occurring in the HBL during production

Example 2: Incoming Seismic Wave with 20^{o} Angle of Incidence

In this example we consider a VSP configuration with the same vertical string of receivers as in the first example, but now the angle of incidence for the incoming seismic wave is 20 degrees (relative to vertical). This allows for creation of converted shear waves, a process in which some energy is converted from the incident P-wave to reflected and transmitted S-waves.

A comparison of the waveforms simulated before and 20 months after the start of production is shown for one rock physics model (Case A) in Figure 10. Both the vertical and horizontal components are shown. The vertical component shows both a direct P-wave and a reflected P-wave (Figure 10a), similar to the previous example, while the horizontal component shows the presence of transmitted and reflected S-waves generated from the incident P-wave. For the case shown in Figure 10, the S-waves are small or not present at the onset of production, but their amplitudes increase with time. Similar to the previous example,

the direct and transmitted P-wave amplitude and velocity remain relatively unchanged after one year of production.

Figure 11 shows how the reflected P-wave and the converted S-waves recorded above the HBL at a depth of 355 m vary during production, depending on the rock physics model. The shape of the reflected P-wave changes substantially with time for Case A but changes less for the remaining cases. The reflected P-wave amplitude decreases for all cases (Figure 12a). The amplitude of the first arriving S-wave is initially low for Cases A and B, but then increases with time, while it is initially much higher for Cases C and D. The amplitude of the converted S-wave increases significantly for Cases A and B, while it changes far less in Cases C and D and subsequently changes far less (Figure 12b).

Examining the signal recorded at a single depth below the HBL (Figure 13), we see that the transmitted P-wave remains mostly unchanged (except for a shift in time for Cases B and D), which was already noted, and that the converted S-wave amplitude increases substantially and consistently for all rock physics models, by a factor of 1.5 in Cases C and D, and by a factor of 13 for Cases A and B (Figure 14).

It is interesting to note that there are slight decreases (of approximately 0.9 ms) in the direct P-wave arrival time recorded underneath the HBL. This effect is caused by changes in effective pressure during production. As fluid is removed from the system and the fluid pressure decreases, the effective pressure (defined as the difference between the lithostatic and pore fluid pressure) increases, corresponding to increased values of the frame bulk moduli K_{dry} and G_{dry}, and thus of the sediment mixture (Dvorkin et al., 1999). There is a competing effect between, on the one hand, the increasing velocities due to the decreasing effective pressure and, on the other hand, the decrease in velocities due to the decreasing hydrate saturation (and increased gas saturation). For all rock physics models, the changes in the direct P-wave arrival are small. Though the arrival time is slightly lower (on the order of

$1.5x10^{-3}$ ms) for Cases B and D, since the P-wave velocities in the HBL increase most in these cases. The decreases in P-wave velocities in the HBL in Cases A and C are mostly balanced by the increases in P-wave velocities in the underlying aquifer (given that the seismic wave passes through both the HBL and the underlying aquifer). However, as discussed above, the changes in the converted S-wave are more substantial for all rock physics models.

Regardless of the rock physics model that is assumed, there are significant changes in the seismic signal when comparing those waveforms simulated before and during production in the HBL. The most reliable indicators of such changes appear to be converted S-waves recorded above and below the HBL, and the reflected P-wave recorded above the HBL.

It should be noted that, if additional site-specific data become available, a more conclusive analysis can be performed with a more accurate model that considers signal-to-noise issues.

Conclusions

In this work we examine the seismic signatures of changes in hydrate accumulations that are predicted to occur during production of natural gas, via time-lapse VSP simulations. We demonstrate that different grain-scale hydrate accumulation types—which correspond to different rock-physics models—result in different time-dependent changes in observed seismic waves. A modeling study such as this is made possible through the coupled simulation of (1) large-scale production in hydrate accumulations and (2) time-lapse geophysical surveys, in this case VSP measurements. We describe the modeling procedure and present some preliminary results.

We consider a simplified oceanic hydrate reservoir model, based on a hydrate accumulation in the Gulf of Mexico, which is thought to represent a promising target for production. Previous modeling of gas production from such an accumulation revealed the

occurrence of several effects that are likely to cause changes in the seismic signature. For example, the descending and ascending dissociating HBL interfaces are expected to change the arrival times and amplitudes of reflected energy, and the decreasing hydrate saturation and increasing gas and aqueous-phase saturations, are also likely to affect the seismic signal. How the signal is affected depends on a number of factors, such as the seismic survey frequency (specifically the wavelength of the propagating energy relative to the thickness of the HBL and underlying aquifer), the depth of the HBL, the contrast in elastic properties between the overburden or background material and the HBL, the position of the sources and receivers. Most importantly, the feasibility of using geophysical measurements depends on rock physics relationships.

In this study, we focused on seismic VSP as the geophysical monitoring method. It is worth noting, however, that while the current study only considers one type of seismic measurement, the general approach for examining possible geophysical signatures in a hydrate reservoir undergoing production can easily be extended to other seismic methods and additional geophysical methods, such as electromagnetic methods. For a normally incident VSP measurement (Example 1), the P-wave energy that was transmitted through the HBL remained nearly constant during the production simulation, making it an unreliable indicator for changes in hydrate accumulations during production. Changes in the amplitude of the reflected P-wave were more significant, though still relatively small (except for in the case of one rock physics model). When considering a VSP configuration with an increased angle of incidence of 20 degrees (Example 2), significant changes in the waveforms were observed before and during production in the HBL, regardless of the rock physics model that was considered. The most reliable indicators of such changes appear to be the following: (1) the converted transmitted S-waves recorded below the HBL; (2) the converted reflected S-waves recorded above the HBL; and (3) the reflected P-wave recorded above the HBL. The

presence of converted S-waves generated as the P-wave travels through the aquifer containing the HBL and underlying water-filled zone was found to be advantageous for all rock physics models.

Overall, this study indicates that seismic methods such as VSP have good potential for detecting changes in hydrate accumulations brought about during natural gas production. Although the current study is based upon an idealized reservoir model and simulations, the above conclusions can be used as a guide for continued efforts in determining seismic signatures that will be most useful for monitoring hydrate accumulations during gas production. A more conclusive analysis, including consideration of the magnitudes of these signatures over background noise, should be performed with a more realistic reservoir model based on site-specific data, and with a more sophisticated model for seismic wave propagation.

Acknowledgments

This work was supported by the Assistant Secretary for Fossil Energy, Office of Natural Gas and Petroleum Technology Laboratory, under the U.S. Department of Energy, Contract No. DE-AC02-05CH11231. The authors are indebted to Matt Reagan for his careful review. The first author would like to acknowledge the support of a Professional Development Grant from the Earth Sciences Division, Lawrence Berkeley National Laboratory.

References

Andreassen, K., Hart, P.E., MacKay, M. 1997. Amplitude versus offset modeling of the bottom simulating reflection associated with submarine gas hydrates. *Marine Geology* **137**: 25-40.

Helgerud, M. B., Dvorkin, J., Nur, A., Sakai, A., Collett, T. 1999. Elastic-wave velocity in marine sediments with gas hydrates: Effective medium modeling. *Geophys. Res. Lett.* **26**(13): 2021–2024.

Carcione, J. M., and Gei, D. 2004. Gas-hydrate concentration estimated from P- and S-wave velocities at the Mallik 2L-38 research well, Mackenzie Delta, Canada. *Journal of Applied Geophysics* **56**(1): 73–78.

Carcione, J.M., D. Kosloff, and Kosloff, R., 1988. Wave propagation in a linear viscoelastic medium. *Geopysics J.* **95**: 597-611.

Collett, T.S., Lee, M.W. 2006. Well Log Analysis: Tiger Shark AC 818 No. 1, U.S. Geological Survey, internal memo.

Dvorkin, J., Prasad, M. Sakai, A. 1999. Elasticity of marine sediments: Rock physics modeling. *Geophys. Res. Lett.* **26**(12): 1781:1784.

Ecker, C., Lumlet, D. Dvorkin, J., Nur, A. 1996. Structure of hydrated sediments from seismic and rock physics, *Proc., 2nd International Conference on Natural Gas Hydrates*, published by PROGEP-NGH conference secretariat, p. 491-498, Toulouse,F rance, 1996.

Ecker, C., Dvorkin, J., Nur, A. 1998. Sediments with gas hydrates: Internal structure from seismic AVO. *Geophysics* **68**: 1659-1669.

Ecker, C. Dvorkin, J. Nur, A. 2000. Estimating the amount of gas hydrate and free gas from marine seismic data. *Geophysics* **65**(2): 565–573.

Gassmann, F. 1951. Uber die Elastizitaet poroser Medien. *Vierteljahrsschrift der Naturforschenden Gesselschaft* **96**:1-23.

Guerin, G., Goldberg, D., Meltser, A. 1999. Characterization of in situ elastic properties of gas hydrate-bearing sediments on the Blake Ridge. *J. Geophys. Res.* **104(B8)**: 17,781–17,795.

Guerin, G., Goldberg, G. 2002. Sonic waveform attenuation in gas hydrate-bearing sediments from the Mallik 2L-38 research well, Mackenzie Delta, Canada. *J. of Geophys. Res.* **107**(B5): 2088, doi: 10.1029/2001JB000556.

Guerin, G., Goldberg, G. 2005. Modeling of acoustic wave dissipation in gas hydrate-bearing sediments. *Geochemistry, Geophysics, Geosystems* **6**: Q07010, doi: 10.1029/2005GC000918.

Helgerud, M., Dvorkin, J. Nur, A. Sakai, A. Collett, T. 1999. Elastic-Wave Velocity in Marine Sediments with Gas Hydrates: Effective Medium Modeling. *Geophys. Res. Lett.* **26**(13): 2021-2024.

Hill, R. 1952. The elastic behavior of crystalline aggregate. *Proc. Phys. Soc. London* **A65**: 249-354.

Hyndman, R.D., Spence, G.D. 1992. A seismic study of methane hydrate bottom simulating reflectors. *Journal of Geophysical Research* **97**: 6683-6698.

Kowalsky, M.B., and Moridis, G. J. 2007. Comparison of kinetic and equilibrium reactions in simulating the behavior of gas hydrates. *Energy Conversion and Management* **48**: 1850–1863, doi:10.1016/j.enconman.2007.01.017.

Kvenvolden, K.A. 1994. Natural gas hydrate occurrence and issues, in *International Conference on Natural Gas Hydrates*, edited by E.D. Sloan, J. Happel, and M.A. Hnatow, Ann. N Y. Acad. Sci. **715**: 232-246.

Kvenvolden, K. A. 2002. Methane hydrate in the global organic carbon cycle. *Terra Nova* **14**: 302–306.

Lee, M.W., Hutchinson, D.R., Collett, T.S., Dillon W.P. 1996. Seismic velocities for hydrate-bearing sediments using weighted equation, *J. Geophys. Res.* 101(B9): 20,347–20,358.

Lee, M.W. 2002. Biot-Gassmann theory for velocities of gas hydrate bearing sediments, *Geophysics* **67**(6):1711-1719.

Lee, M.W. 2007. Velocities and attenuations of gas hydrate-bearing sediments: U.S. Geological Survey Scientific Investigations Report 2007-5264, 11 pages.

Makogen, Y.F. 1997. *Hydrates of hydrocarbons*. Penn Well Publishing, Tulsa.

Moridis, G.J., Kowalsky, M.B. Pruess, K. 2008. TOUGH+HYDRATE v1.0 User's Manual: A code for the Simulation of System Behavior in Hydrate-Bearing Geologic Media, Report LBNL 00149E, Lawrence Berkeley National Laboratory.

Moridis, G.J., Kowalsky, M.B. 2007. Response of oceanic hydrate-bearing sediments to thermal stresses. *SPE Journal* **12**(2): 253-268.

Moridis, G., Kowalsky, M.B., Pruess, K. 2007. Depressurization-induced gas production from class 1 hydrate deposits, *SPE Reservoir Evaluation and Engineering* **10**(5), 458-481.

Moridis, G.J., Reagan, M. T. 2007. Gas Production From Oceanic Class 2 Hydrate Accumulations. Paper OTC 18866 presented at the 2007 Offshore Technology Conference, Houston, Texas, April 30–May 3, 2007.

O'Brien, J., Kilbride F., and Lim, F. 2004. *The Leading Edge* **23**(11): 1178–1184, DOI: 10.1190/1.1825943

Rossi, G., Gei, D., Boehm, G., Madrussani, G., Carcione, J. 2007. Attenuation tomography: An application to gas-hydrate and free-gas detection. **55**(5): 655-669.

Ruess, A. 1929. Berechnung der Fliessgrenzev von Mischkristallen auf Grund der Plastizitaetsbedinungen fuer Einkristalle. *Ztschr. fuer Angewandte Math. u. Mech.* **9**:49-58.

Sloan, E. D. 1998. *Clathrate hydrates of natural gas*. Marcel Decker, Inc., New York.

Smith, S., Boswell, R., Collett, T., Lee, M., Jones, E. 2006. Alaminos Canyon Block 818: A Documented Example of Gas Hydrate Saturated Sand in the Gulf of Mexico, *Fire In The Ice*, NETL Methane Hydrates R&D Program Newsletter, Fall 2006.

Spangenberg, E. 2001. Modeling of the influence of gas hydrate content on the electrical properties of porous sediments. *Journal of Geophysical Research* **106**(B4): 6535-6548.

Sun, Y.F., Goldberg, D. 2005. Dielectric method of high-resolution gas hydrate estimation, *Geophys. Res. Lett.*, 32, L04313, doi:10.1029/2004GL021976.

Winters, W.J., Waite, W.F., Mason, D.H., Gilbert, L.Y., Pecher, I.A. 2007. Methane gas hydrate effect on sediment acoustic and strength properties. *J. Petroleum Science and Engineering* **56**: 127-135.

Wood, A.B. 1941. A textbook of sound, Macmillian, New York, 578 pages.

Wyllie, M.R.J., Gregory, A.R., Gardner, G.H.F. 1986. An experimental investigation of factors affecting elastic wave velocities in porous media. *Geophysics* **51**: 1285-1290.

Yuan, T., Hyndman, R.D., Spence, G.D., Desmons, B. 1996. Velocity structure of a bottom-simulating reflector and deep sea gas hydrate concentrations on the Cascadia continental slope. *Journal of Geophysical Research* **101**:13655-13671.

Xu, M., McMechan, G.A. 1998. Efficient 3-D viscoelastic modeling with application to near-surface land seismic data, *Geophysics* **63**(2): 601-612.

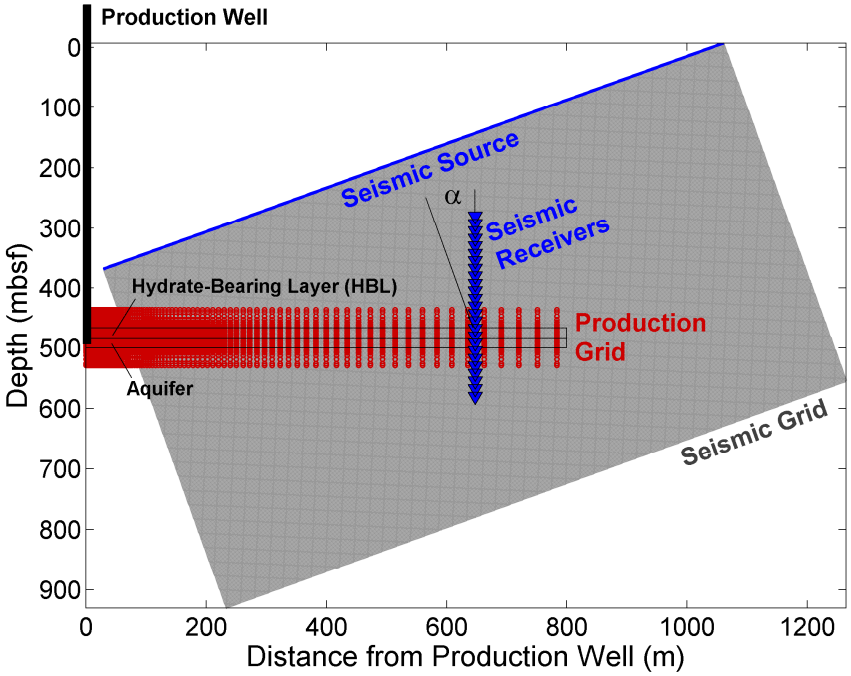

Figure 1. Geometry of marine hydrate-bearing system and numerical grids used to simulate production of natural gas from the hydrate bearing-layer (red grid) and to simulate of time-lapse seismic surveys (gray grid). The production simulation uses a radial coordinate system, while the seismic simulations use a Cartesian coordinate system that cuts through the radial production model. The angle α between the production grid and the seismic grid determines the angle of the incoming seismic wave relative to the HBL. In the first example $\alpha = 0^o$, and in the second example $\alpha = 20^o$, with the seismic grid rotated accordingly.

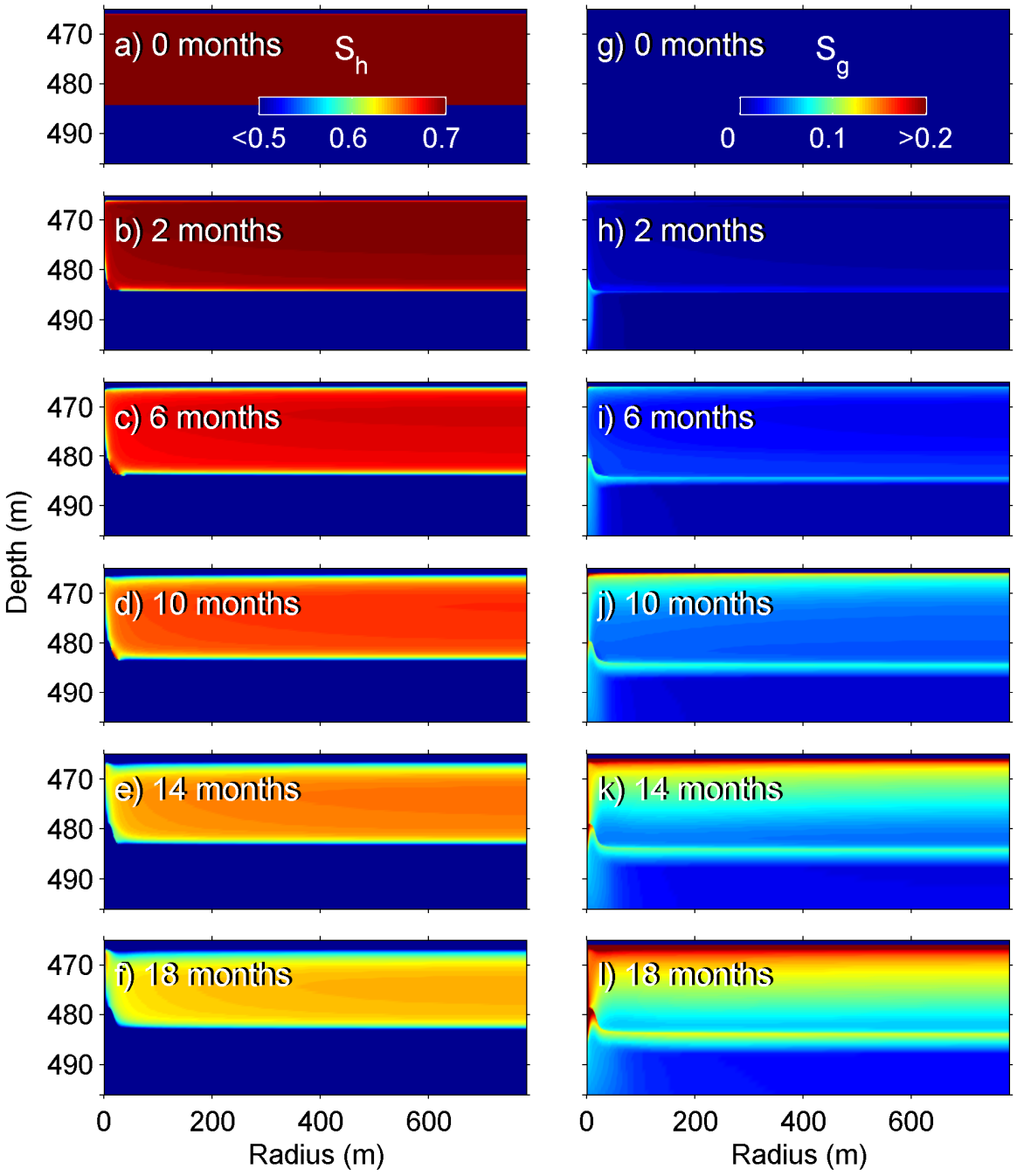

Figure 2. Distributions of gas hydrate saturation (a-f) and gas saturation (g-l) from production simulation for increasing times after the beginning of production (0, 2, 6, 10, 14, and 18 months, respectively). The color scales for S_h and S_g are clipped below 0.5 and above 0.2, respectively, to improve visualization. For reference, note that the top and bottom of the HBL are at 466 m and 485 m, respectively, while the top and bottom of the underlying aquifer are at 485 m and 500 m, respectively.

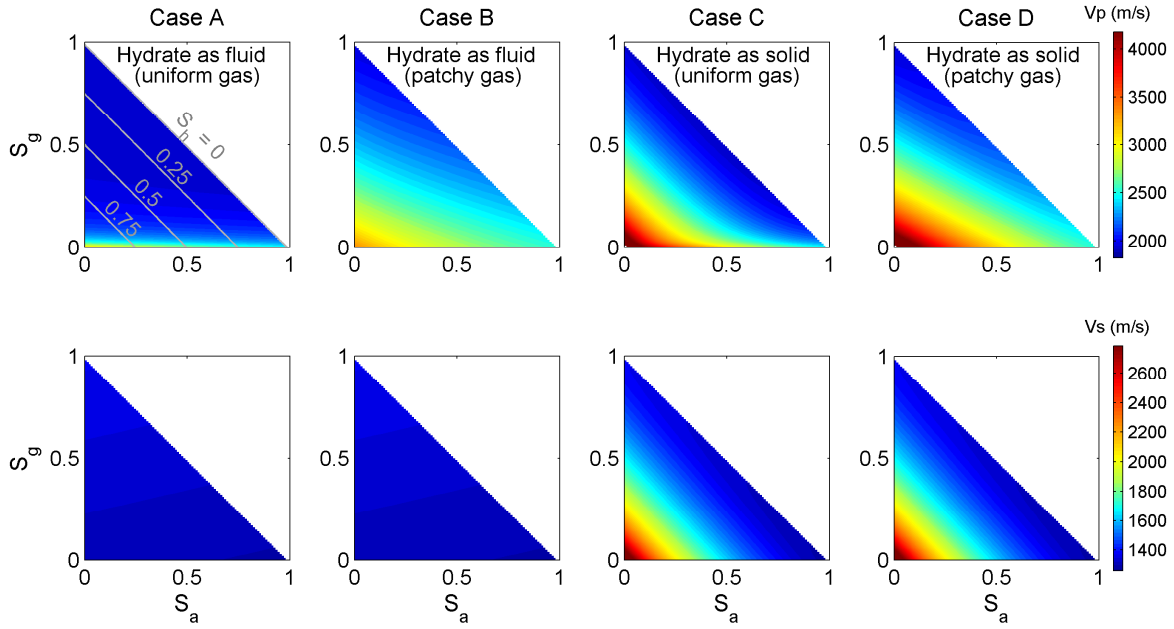

Figure 3. Seismic velocities for Cases A-D of the rock physics models considered in this study. The P-wave velocity (V_p) and S-wave velocity (V_s) are shown along the top and bottom rows, respectively, as a function of aqueous-phase saturation (S_a), gas-phase saturation (S_g), and hydrate-phase saturation (S_h), defined as the volumes of S_a, S_g, and S_h, respectively divided by the total volume of the hydrate-, aqueous-, and gas-phase components. S_a and S_g are given on the x-axis and y-axis, respectively, and the isolines of S_h are shown in the upper left plot.

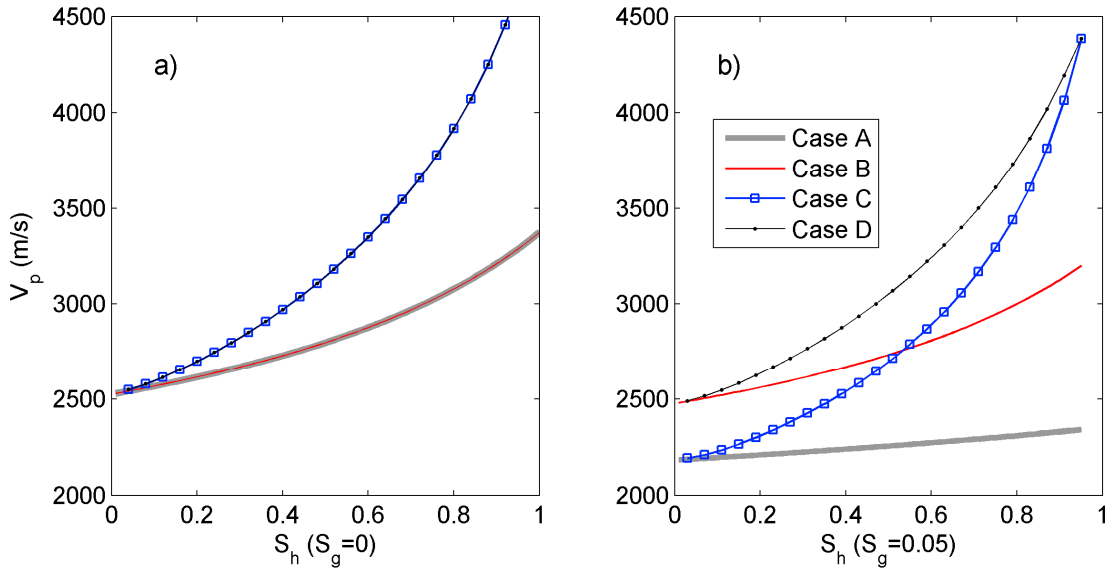

Figure 4. P-wave velocity (V_p) of sediment mixture for Cases A-D as a function of hydrate saturation with (a) no gas present (S_g = 0), and (b) a small amount of gas present (S_g = 0.05). Recall that S_a = 1-S_h-S_g. Note that in (b), when S_g = 0.05, the maximum possible value of S_h is 0.95.

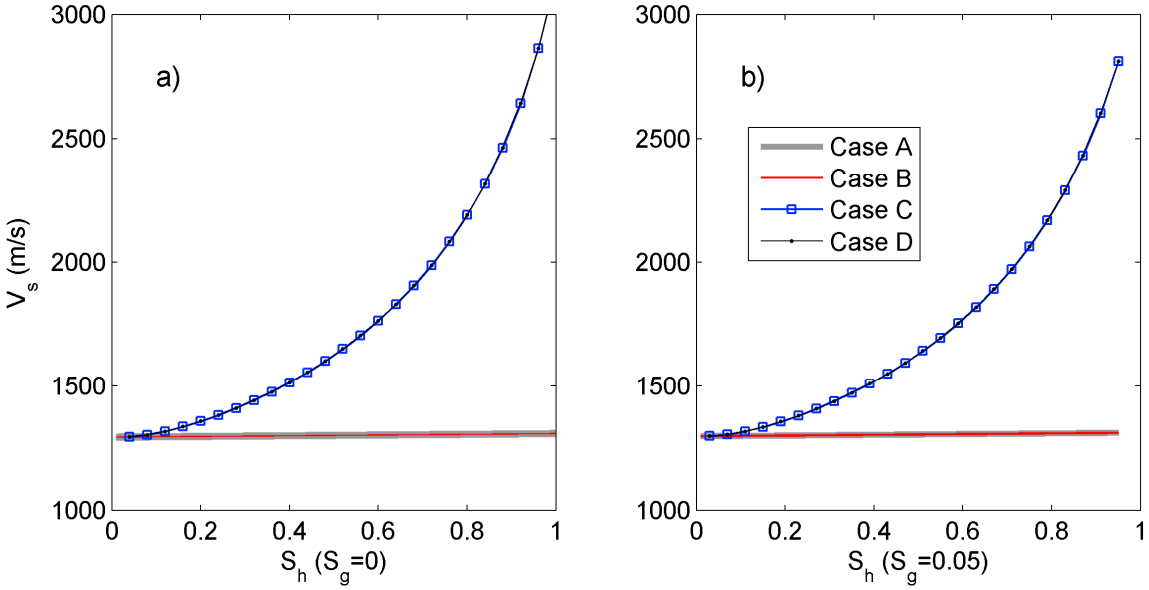

Figure 5. S-wave velocity (V_s) of sediment mixture for Cases A-D as a function of hydrate saturation with (a) no gas present (S_g = 0), and (b) a small amount of gas present (S_g = 0.05). Recall that S_a = 1-S_h-S_g. Note that in (b), when S_g = 0.05, the maximum possible value of S_h is 0.95.

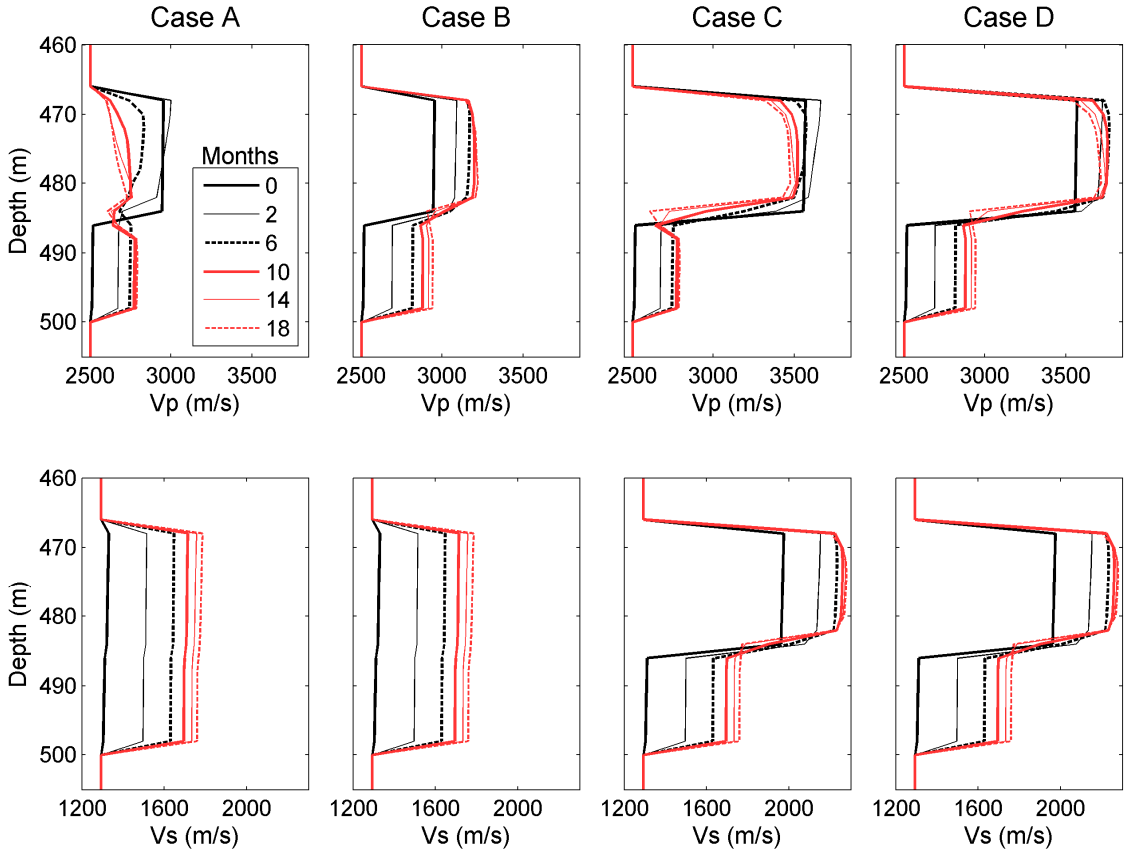

Figure 6. P-wave velocity (top) and S-wave velocity (bottom) as a function of time during the production simulation for Cases A-D of the considered rock physics models. For reference, note that the top and bottom of the HBL are at 466 m and 485 m, respectively, while the top and bottom of the underlying aquifer are at 485 m and 500 m, respectively.

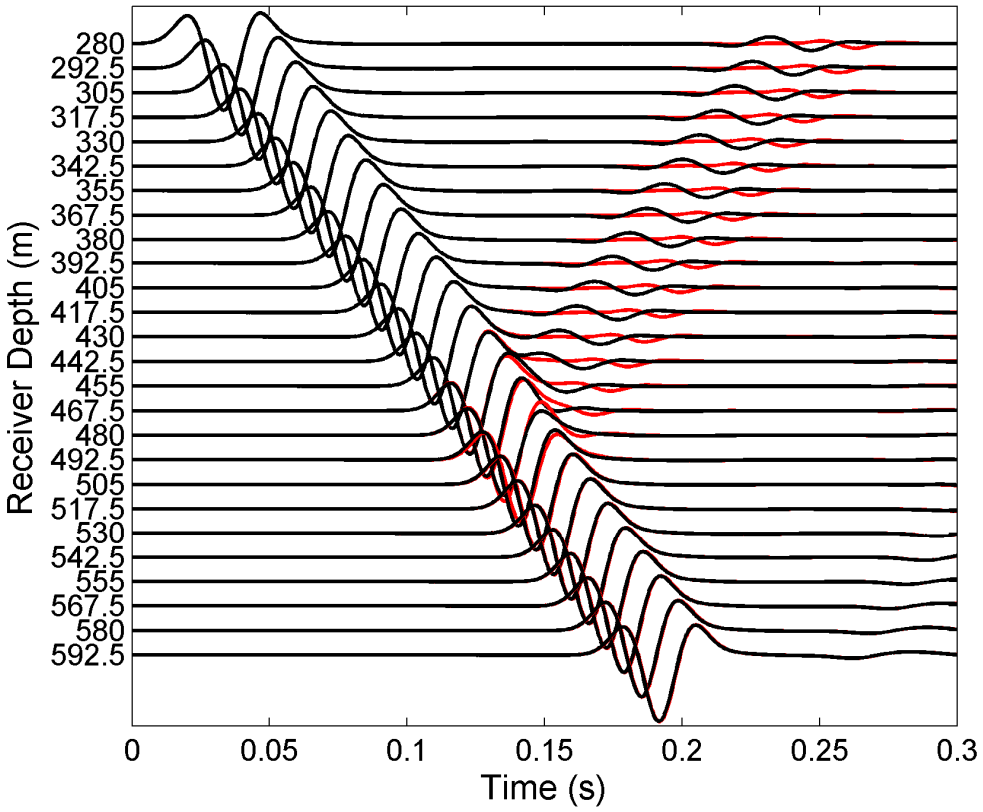

Figure 7. Simulated VSP survey for Case A of Example 1 at two survey times corresponding to 0 and 18 months (black and red, respectively) after the start of production.

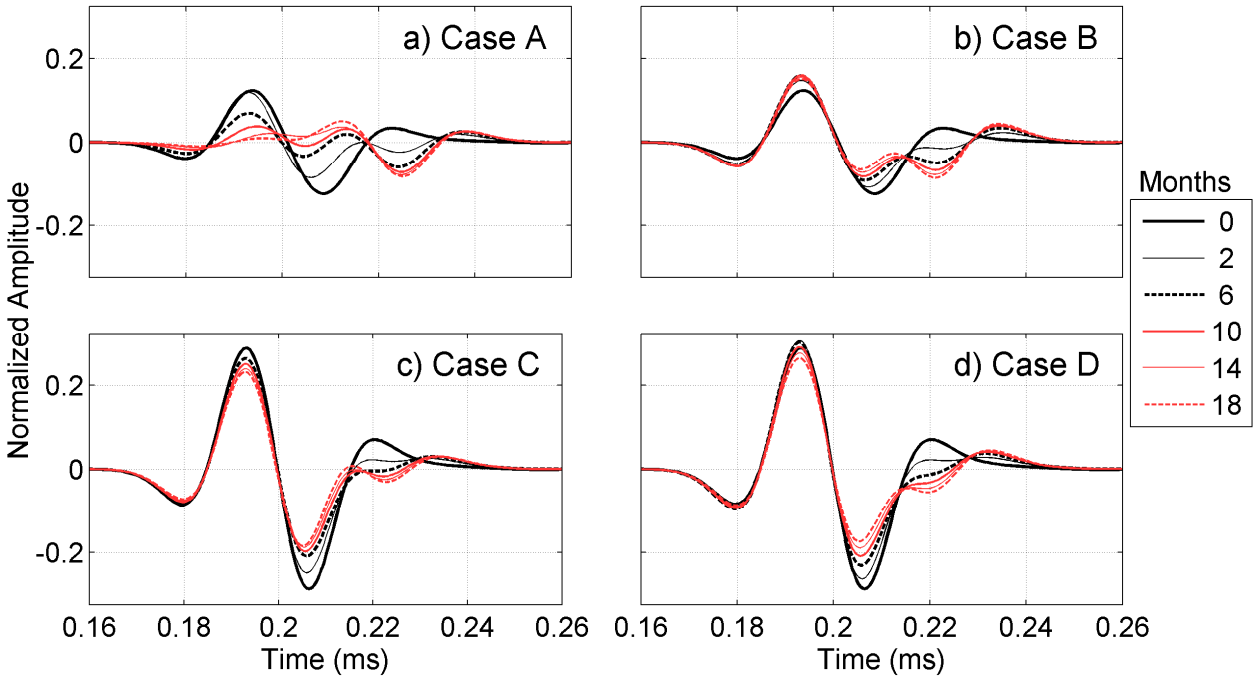

Figure 8. Seismic signal (reflected P-wave) recorded above the HBL at a depth of 355 m in Example 1. Waveforms are shown at six survey times (0, 2, 6, 10, 14, and 18 months after the start of production) for each rock physics model.

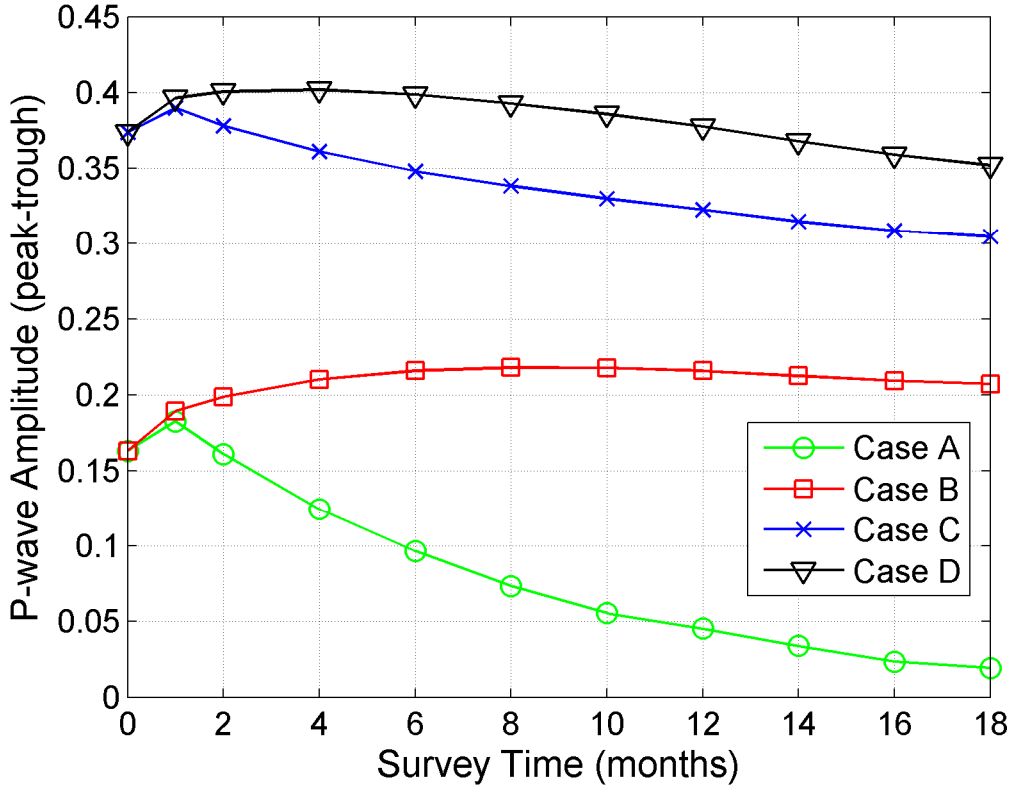

Figure 9. Amplitude of seismic signal (reflected P-wave) recorded above HBL at a depth of 355 m in Example 1 for each rock physics model as a function of survey time.

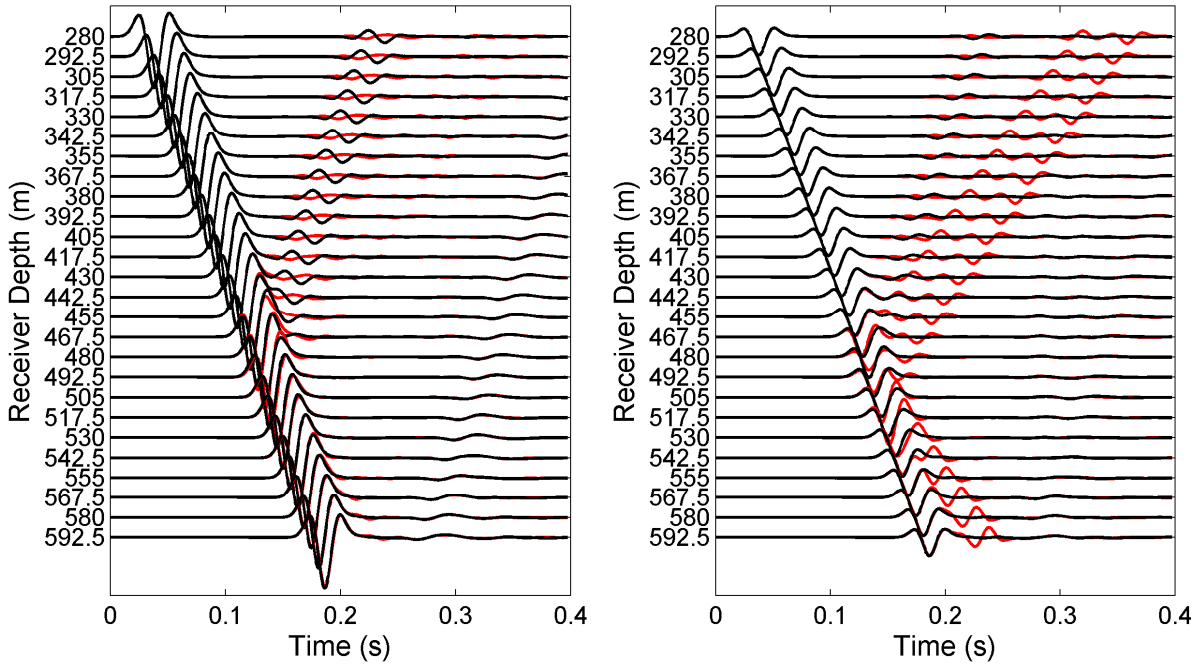

Figure 10. Simulated VSP survey for Case A of Example 2 at two survey times corresponding to 0 and 18 months (black and red, respectively) after the start of production. The a) vertical and b) horizontal components of the signal are shown.

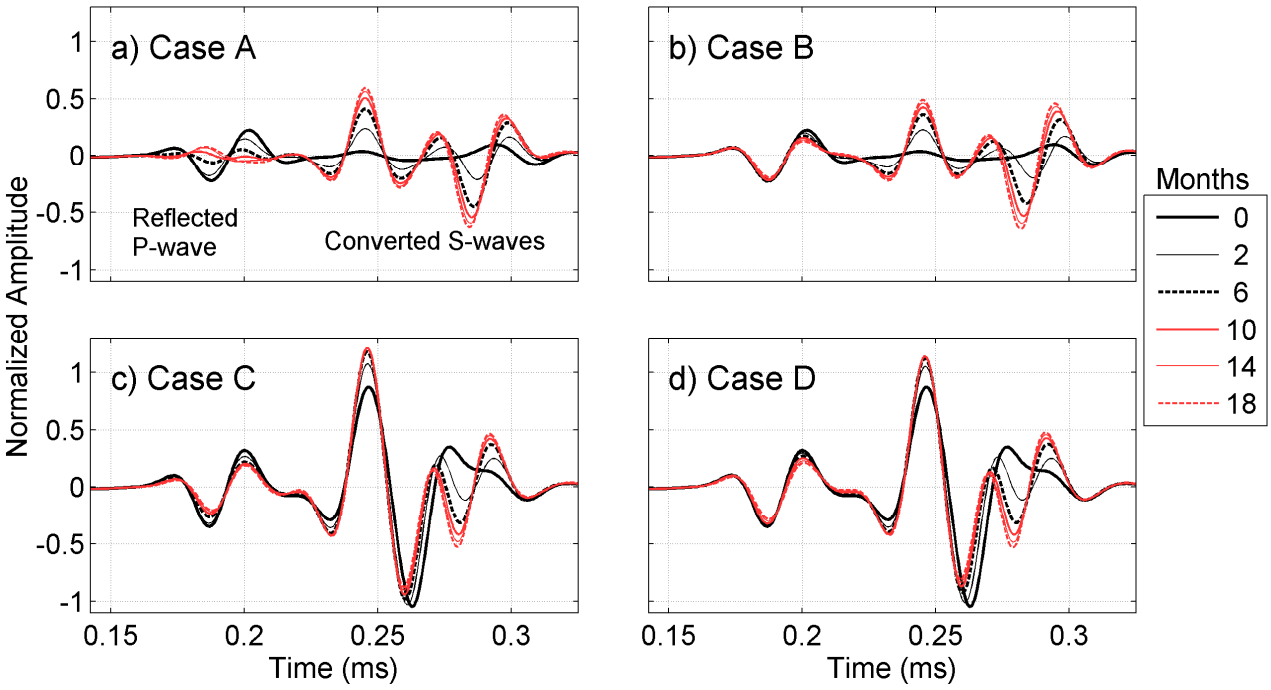

Figure 11. Seismic signal (portion showing horizontal component of the reflected P-wave and converted S-waves) recorded above the HBL at a depth of 355 m in Example 2. Waveforms are shown at six survey times (0, 2, 6, 10, 14, and 18 months after the start of production) for each rock physics model.

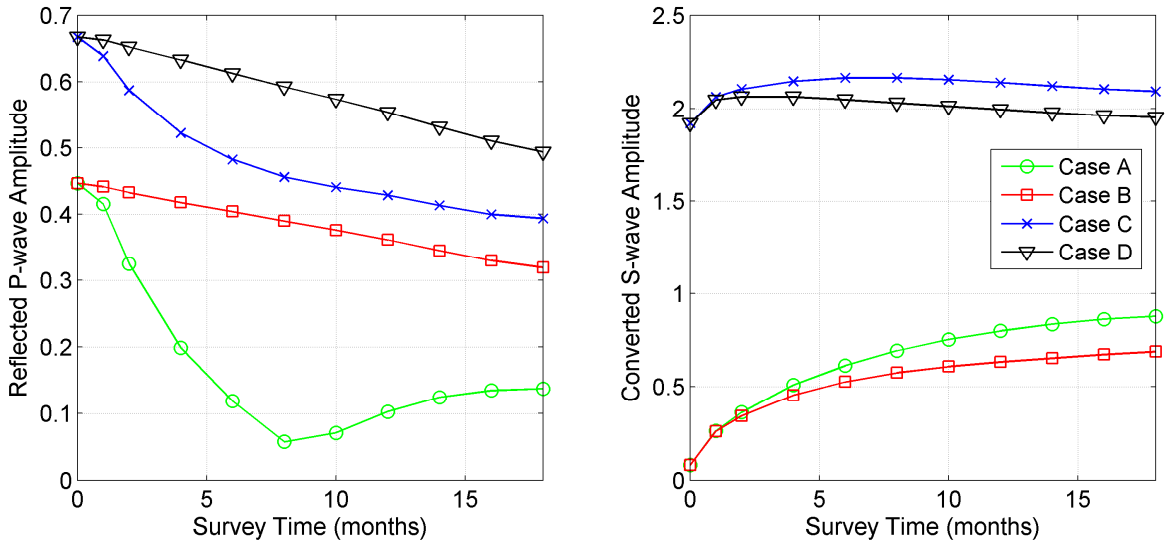

Figure 12. Amplitude of seismic signal (portion showing the horizontal components of the reflected P-wave and converted S-waves; refer to Figure 11) recorded above the HBL at a depth of 355 m in Example 2 for each rock physics model as a function of survey time.

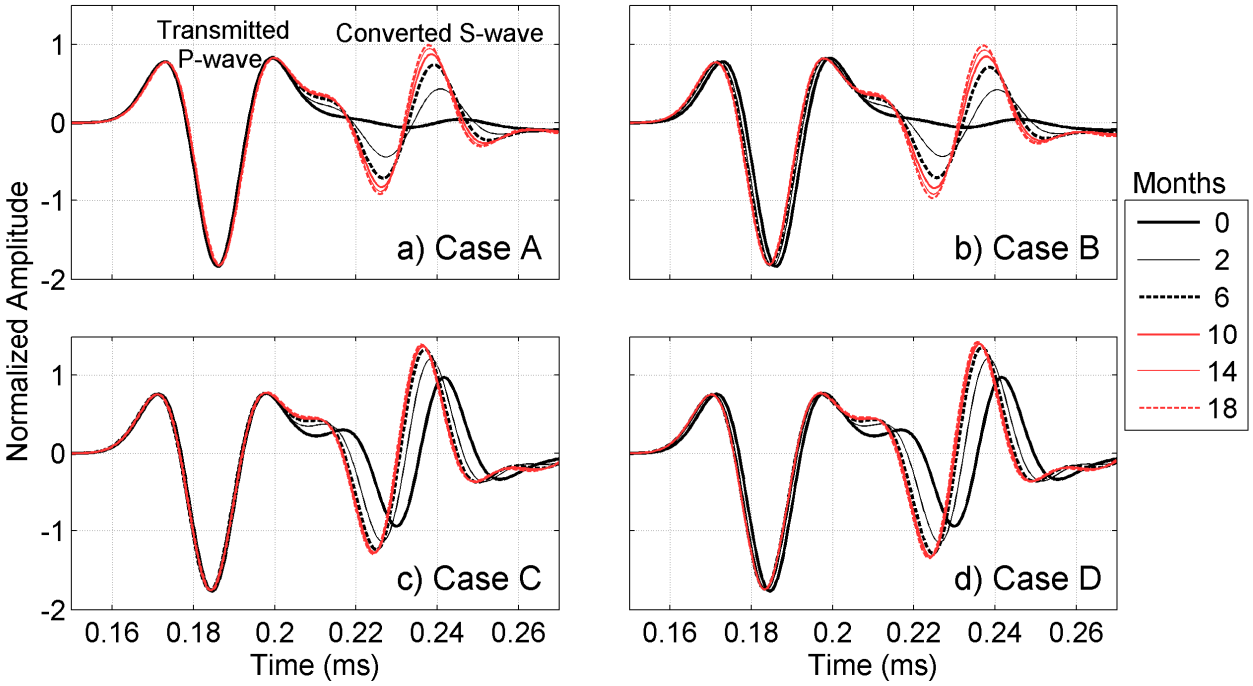

Figure 13. Seismic signal (portion showing horizontal component of the reflected P-wave and converted S-waves) recorded below the HBL at a depth of 592.5 m in Example 2. Waveforms are shown at six survey times (0, 2, 6, 10, 14, and 18 months after the start of production) for each rock physics model.

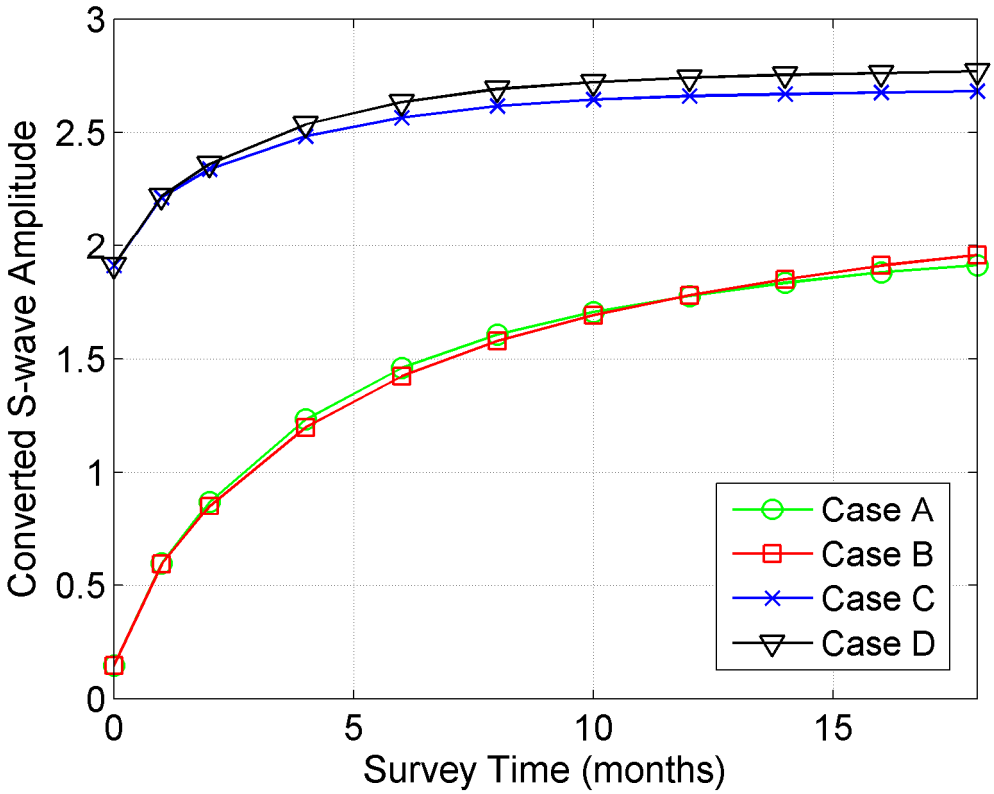

Figure 14. Amplitude of seismic signal (portion showing the horizontal components of the converted S-wave; refer to Figure 13) recorded below the HBL at a depth of 592.5 m in Example 2 for each rock physics model as a function of survey time.